Surface & Coatings Technology 464 (2023) 129545

Contents lists available at ScienceDirect

Surface & Coatings Technology

journal homepage: www.elsevier.com/locate/surfcoat

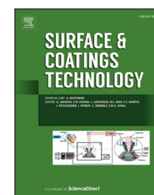

Full length article

Electrical properties and thermistor behavior of TiAlN thin films deposited by combinatorial sputtering

Bruno Martins [a,b,*], Carlos Patacas [a,b], Albano Cavaleiro [a,b], Pedro Faia [c], Oleksandr Bondarchuk [e], Filipe Fernandes [a,b,d]

[a] IPN - LED&MAT - Instituto Pedro Nunes, Laboratório de Ensaios, Desgaste e Materiais, Rua Pedro Nunes, 3030-199 Coimbra, Portugal
[b] University of Coimbra, CEMMPRE, ARISE, Department of Mechanical Engineering, Rua Luís Reis Santos, 3030-788 Coimbra, Portugal
[c] University of Coimbra, CEMMPRE – Electrical and Computer Engineering Department, FCTUC, Polo 2, Pinhal de Marrocos, Coimbra 3030-290, Portugal
[d] ISEP - Polytechnic of Porto, Rua Dr. António Bernardino de Almeida, 4249-015 Porto, Portugal
[e] International Iberian Nanotechnology Laboratory (INL), Avenida Mestre Jose Veiga, 4715-330 Braga, Portugal

ARTICLE INFO

Keywords:
NTC thin-film thermistor
Reactive sputtering
Nitride semiconductors
Impedance spectroscopy
Sheet resistance

ABSTRACT

A combinatorial deposition was performed by direct current magnetron sputtering (DCMS) to develop $Ti_{1-x}Al_xN$ thin films with different Ti/Al ratios and investigate the electrical response to temperature. The crystal structure as a function of the x was studied by X-ray diffraction, and sheet resistance response was measured up to 200 °C. From x = 0.16 to x = 0.56, the film shows an fcc phase with Al in solid solution in the TiN matrix, whilst, from x ≥ 0.69, a mixture of hcp (AlN) and fcc phases is observed. A negative temperature coefficient (NTC) thermistor behavior was found from x = 0.21 onwards, and a maximum sensitivity β of 1600 K was observed for x = 0.56 and 0.69. One fcc sample (x = 0.46) was selected to analyze the chemical states by X-ray photoelectron spectroscopy and the impedance behavior with the temperature by electrical impedance spectroscopy. The crystal structure, bond states and impedance analysis were compared with an AlN thin film. It is concluded that the conduction mechanism for x = 0.46 is based upon electron hopping, and the effect of the grain boundary is more relevant than the grain at low temperatures. We demonstrate that it is possible to use TiAlN as an NTC-thermistor with different crystal structures and chemical compositions.

1. Introduction

Contact surfaces between moving bodies will always produce friction and, consequently, develop a temperature gradient, which inevitably will lead to component failure if not adequately addressed. The industry is seeking solutions to measure the temperature in-situ on those contacts. Transition metal nitrides (thin films) have been used and studied for years for tribological applications [1]. For instance, TiAlN thin film has been commonly used in cutting tools due to its high-temperature behavior, high oxidation resistance, high hardness and high corrosion resistance, which improve the tool life during cutting processes [1,2]. On the other hand, nitrides are also being applied for sensing applications. Mitsubishi materials research group [3–5] developed an (NTC) thermistor – resistive temperature sensor where the electrical resistance decreases exponentially with temperature – by substituting Al per Ti in the wide band-gap semiconductor AlN. As a result, several patent applications regarding metal nitrides for temperature sensors intended to produce flexible temperature sensors were submitted [6–8]. The common axis regarding these patents is the hexagonal wurtzite single-phase crystal structure and the chemical composition of $Ti_xAl_yN_z$; $0.7 \leq y(x + y) \leq 0.95$; $0.4 \leq z \leq 0.5$; $x + y + z = 1$.

Thermistors with NTC characteristics are known for their fast response, high sensitivity and low price [9,10]. Hence, they are suitable for temperature monitoring in automotive electronics, 3D printers and house appliances [9–13]. Positive temperature coefficient thermistors (PTC) are uncommon and less attractive to the research community; nevertheless, they are still used in critical applications such as circuit breakers or circuit temperature compensation. The temperature sensor selection is based on their sensitivity or thermal index, β, as well as on their temperature coefficient of resistance (TCR) and resistance at room temperature, R25. Most NTC sensors are established as transition metal oxides semiconductors composed of Mn-Co-Ni-O with spinel structure AB_2O_4. The conduction mechanism is classified as electron hopping through cation pairs located in B or A lattice sites [9–15].

* Corresponding author at: IPN - LED&MAT - Instituto Pedro Nunes, Laboratório de Ensaios, Desgaste e Materiais, Rua Pedro Nunes, 3030-199 Coimbra, Portugal.
E-mail address: brunomartins@ipn.pt (B. Martins).

https://doi.org/10.1016/j.surfcoat.2023.129545
Received 10 January 2023; Received in revised form 28 March 2023; Accepted 16 April 2023
Available online 28 April 2023
0257-8972/© 2023 Elsevier B.V. All rights reserved.

Regarding transition metal nitrides, Fujita et al. [3] stated that for $Al_{1-x}Ti_xN$ where x < 0.3 %, it is impossible to achieve NTC functionality. They concluded that the β value depends on both the Ti content and the N defects, and the dominant conduction mechanism is via sp3 covalent bonding in the wurtzite structure. Recently, the same authors confirmed that it is possible to develop TiAlN with a cubic structure with high Al content, suggesting two conduction mechanisms depending on the temperature through i) valence band at high temperatures and ii) variable range hopping at low temperatures. Yoshikawa et al. [4] also reported that the cubic TiAlN films exhibit p-type semi-conductivity and that hopping conduction occurs at low temperatures. Authors tend to overlook the cubic form of TiAlN in favor of hexagonal crystal structure due to its low sensitivity (30–750 K) [3,6–8]. However, this limits the potential applications of the TiAlN in harsh mechanical environments where high temperatures are typically present. Despite its low sensitivity, the cubic TiAlN may still be suitable for high-temperature sensing applications due to the exponential relationship between sensitivity and temperature. As a result, the potential use of cubic TiAlN as a temperature sensor cannot be discarded.

The Al substitution by Ti in the AlN to achieve NTC characteristics and the theory for the conduction mechanism are generally recognized by the scientific community. However, the Ti/Al ratio and the crystal structure, for which semiconductor properties can be developed, demand further insights. In addition, until today, the role of the microstructure – grain and grain boundaries – in the electrical properties still needs to be understood. To tackle these questions, TiAlN thin films were deposited by DCMS, with different Ti/Al ratios, using a combinatorial deposition setup in static mode. Firstly, the crystal structure evolution and the thermo-resistive properties of the films were studied. Then, the one composition with NTC properties within the cubic phase was investigated regarding the chemical bond and the electrical impedance response. An AlN wurtzite phase thin film was synthesized by the same deposition technique and used for comparison purposes. This study contributes to understanding the conduction mechanisms in TiAlN films to preview their potential for wear and sensorial functionalities.

2. Materials and methods

For creating a chemical gradient by changing the x content in a $Ti_{1-x}Al_xN$ ternary compound, sputtering equipment equipped with four magnetrons (380 × 175 mm) in a magnetic closed-field configuration in direct current (DC) mode was used. The substrate bias was set to pulsed DC mode in the mid-frequency range. As depicted in Fig. 1, the substrate holder was positioned with a 45° off-axis angle in relation to the Al and Ti targets, while the center of the target erosion track was selected to estimate the angular flux distribution (considering the cosine law for the distribution of atoms flux). Between 0 and 30°, the intensity of the sputtering flux is higher. Also, the substrate holder height was selected to set the position of the silicon substrates (with dimensions around 20 × 20 mm) in the middle of the height of the vacuum chamber. The chamber's distances and layout positioning were conducted and controlled using computer-aided design (CAD) software (Fusion360®).

An AlN film was also deposited to compare the crystal structure, chemical bonding and electrical properties. This film was produced with the same equipment, using two Al targets at an angular position of 180° (facing each other). The AlN deposition was conducted with the substrate holder in rotation mode. All depositions, combinatorial TiAlN and AlN, were performed in reactive mode by introducing a gas mixture of N_2 and Ar into the chamber. The hysteresis effect is well known in reactive sputtering; therefore, the chamber possesses a control loop system [16] which was used to regulate the N_2 flux in the gas mixture, whereas the Ar flux was fixed. A mass flow controller performs the flux

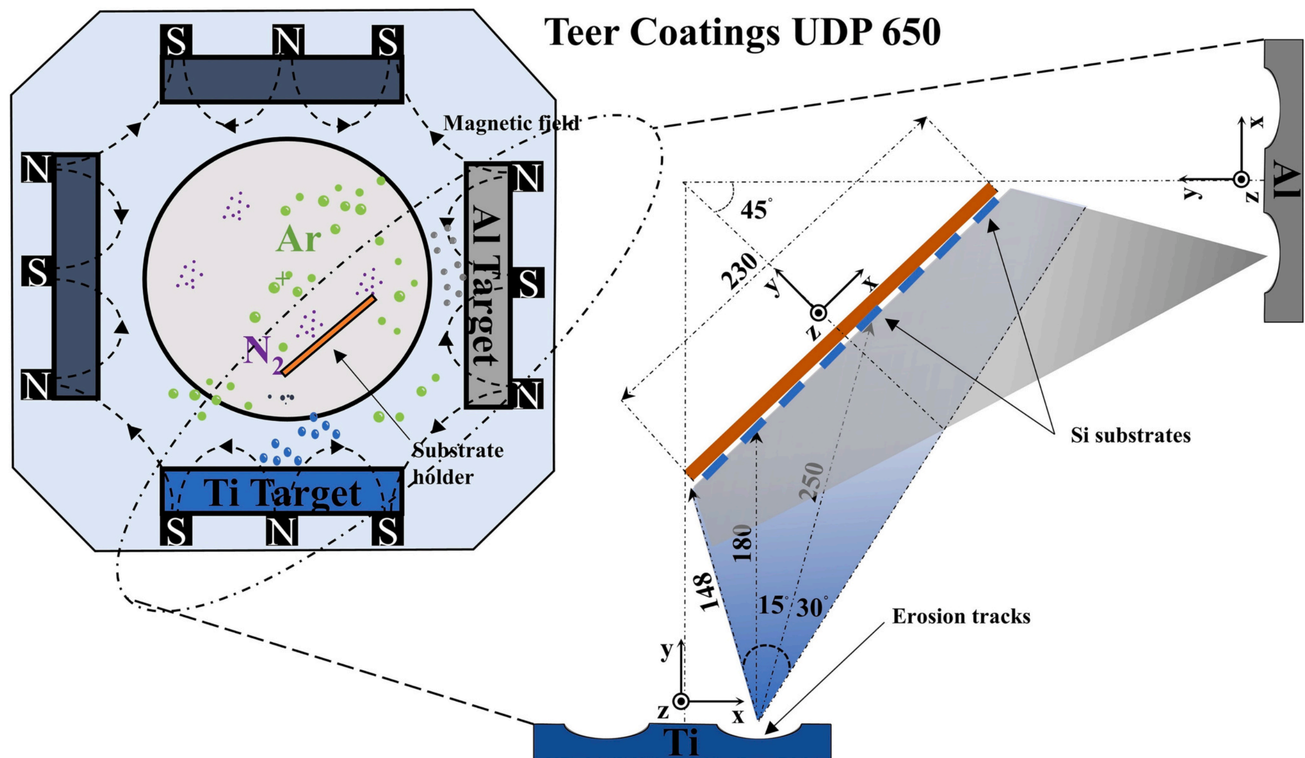

Fig. 1. Schematic layout for the combinatorial deposition of the $Ti_{x-1}Al_xN$ compound with respective dimensions and chamber configuration. Teer Coatings UDP 650 equipment equipped with four targets was used.

Table 1
Main deposition parameters used to produce the films.

	Combinatorial TiAlN	AlN
Ultimate vacuum (Pa)	$< 5 \times 10^{-4}$	$< 5 \times 10^{-4}$
Substrates in-situ cleaning – physical etching		
Substrate bias (V)	−650	−650
Time (min)	30	30
Ar pressure (Pa)	0.1	0.1
Targets power density ($W.cm^{-2}$)	0.15	0.15
Pulse frequency (kHz)	245	245
Reverse time (μs)	1.8	1.8
Deposition procedure		
	TiAlN	AlN
Working pressure (Pa)	≈ 0.21	≈ 0.25
Rotation speed (RPM)	–	10
Al Power density ($W.cm^{-2}$)	≈ 3	≈ 6 (x2)
Ti Power density ($W.cm^{-2}$)	≈ 3	–
Substrate bias (V)	−50	−60
Bias pulse frequency (kHz)	250	250
Bias reverse time (μs)	0.5	0.5
Deposition time (min)	60	60
Target-substrate distance (mm)	–	150
Substrate temperature (°C)	≈ 160	≈ 200

regulation in PID (proportional – integral – derivative) mode based on the working pressure readings obtained by a capacitance sensor.

The Si (111) substrates were cleaned in ultrasonic baths of acetone, alcohol and distilled water (10 min each) and dried with compressed air; then, the substrates were fixed in the substrate holder with silver glue. Finally, the holder was connected to the supports inside the vacuum chamber, and the chamber was pumped down to 5×10^{-4} Pa. Deposition parameters are detailed in Table 1. It is important to note that the deposition starts at room temperature, and the substrate temperature reported is achieved during the deposition as a consequence of the process (measured using a surface thermometer – PTC instruments®).

The coatings' thickness was measured by the ball crater method in a CSEM Calotest® apparatus and confirmed with field-emission scanning electron microscopy (FE-SEM) ZEISS Merlin® of the cross-section of the samples. The crater was performed close to the sample's edges, for not disturbing the electrical characterization to be performed afterwards. The chemical composition was analyzed by energy dispersive X-ray (EDX) technique with a Oxford Instrument combined with SEM. The crystal structure was evaluated by X-ray diffraction (XRD) using a Panalytical X'pert equipment with Co Kα radiation (λ = 0.178897 nm) in conventional Bragg-Brentano geometry. The baseline correction was performed for each XRD spectra sample, while the peaks were fitted using a Pseudo-Voigt function to calculate the peak position (2θ) and the full width at half maximum (FWHM). The peak identification was accomplished using Joint Committee on Powder Diffraction Standards (JCPDS) cards: TiN 087–0628 and AlN 87–1054. The lattice constant was calculated through the interplanar distance or d_{hkl}-spacing using Bragg's law formulae, while the crystallite size was estimated by the Scherrer equation.

The variation of the samples electrical properties with temperature was measured from room temperature to 200 °C by two methods: i) four-point measurement (4 PM) method and ii) electrical impedance spectroscopy (EIS). The 4 PM tests were performed using a four-point probe Ossila equipment capable of measuring sheet resistance between 100 $m\Omega.sq.^{-1}$ to 10 $M\Omega.sq.^{-1}$, with a 1.23 mm probe pitch. The EIS study was carried out using a precision impedance analyzer (Agilent 4294A) with excitation frequencies ranging from 10 kHz to 36 MHz, with a peak voltage of 500 mV. The EIS and 4 PM equipment have distinct heating benches. The Agilent is connected to a cartridge resistor heater, and the Ossila is connected to a high-speed SiC heater; both resistors are PID controlled. With the 4 PM method, it was possible to compute the resistivity through the measured sheet resistance and the film thickness of each composition at room temperature, according to the equation $\rho = R_s \times t$, where ρ is the resistivity, in μΩcm; Rs is the sheet resistance, in $\mu\Omega.sq.^{-1}$, and t is the thickness of the coating, in cm. The Ossila Sheet Resistance V2.0.7.1 software automatically applies the correction factors accounting for the sample geometric parameters [17].

The oxidation state of the elements present in the films was analyzed by X-ray photoelectron spectroscopy (XPS). The test was performed in an ESCALAB 250Xi (Thermo Fisher Scientific) apparatus with a hemispherical analyzer and a monochromated Al Kα (hν = 1486.68 eV) X-ray source at 220 W, operated at 14.6 kV and possessing a 650 μm spot size. XPS spectra were collected at pass energies of 100 eV and 40 eV for survey and individual elements identification (high-resolution spectra), respectively. The energy step for the HR analysis was 0.1 eV: all the XPS peaks were referenced to adventitious carbon C 1s and C—C peak at 284.8 eV. For peak fitting, Shirley-type background subtraction was used in the Origin® software. The samples were not sputter cleaned before the analysis to avoid changes in the structure during ions bombarding/cleaning.

The sensitivity index β, activation energy E_a, and the TCR were calculated for all the chemical compositions. For the β value, the following equation was used:

$$\beta_{[25-100^{\circ}C]} = \frac{ln\left(\frac{R_{T1}}{R_{T2}}\right)}{\left(\frac{1}{T_1} - \frac{1}{T_2}\right)} \quad (1)$$

In Eq. (1), β is in K, and R_{T1} and R_{T2} are the sheet resistances at temperatures T_1 and T_2. TCR was calculated within the same temperature range as the sensitivity, according to Eq. (2):

$$TCR = \frac{R_2 - R_1}{R_1(T_2 - T_1)} \quad (2)$$

where TCR is expressed in $^{\circ}C^{-1}$.

The activation energy was calculated from the Arrhenius plot by determination of the slope between lnRs and 1000/T (T is the absolute temperature in K) in the linear part of the plot, using the expression $E_a = 1000 \times slope \times k$, where E_a is the activation energy in eV, and κ is the Boltzmann constant in eVK^{-1}.

The EIS and XPS measurements were only conducted in the most promising film, considering the crystal structure, chemical range and sensitivity β – and for sample AlN used as a reference in the study.

3. Results and discussion

3.1. Chemical composition and structure

The chemical composition of the films is shown in Table 2. As expected, as the substrates get closer to the Al target, an increase of the Al concentration on the films could be successfully achieved with the

Table 2
Chemical composition of the films by EDX technique. Light elements from contamination, such as O or C, are not shown since the quantities detected are not significant (<2 at.%).

Al/(Al + Ti)	Ti (at.%)	Al (at.%)	N (at.%)
0.16	41.1 ± 0.3	7.9 ± 0.1	51 ± 0.3
0.21	38.7 ± 0.3	10.6 ± 0.1	50.7 ± 0.3
0.3	34.2 ± 0.4	14.5 ± 0.2	51.3 ± 0.3
0.36	30.5 ± 0.4	17.5 ± 0.2	52.0 ± 0.3
0.46	26.5 ± 0.4	22.8 ± 0.2	50.7 ± 0.3
0.56	21.5 ± 0.4	27.4 ± 0.2	51.2 ± 0.3
0.69	15.1 ± 0.4	33.8 ± 0.3	51.1 ± 0.3
0.78	11.0 ± 0.4	38.5 ± 0.3	50.5 ± 0.3
1	–	51.5 ± 0.2	48.5 ± 0.3

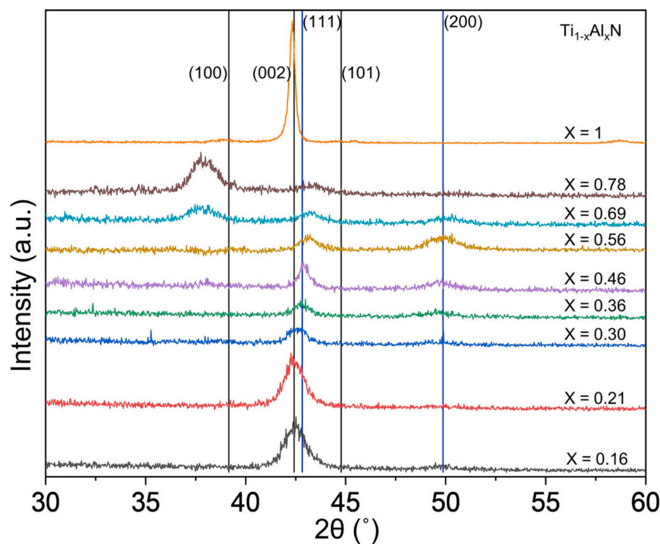

Fig. 2. $Ti_{1-x}Al_xN$ X-ray diffractogram evolution with Al content and respective standard orientations: (100)(002)(101) for AlN, and (111)(200) for TiN. The XRD pattern for AlN is referenced as x = 1. The ICDD card numbers taken as reference are TiN – 87-0633 and AlN 87-1054.

deposition setup shown in Fig. 1. The minimum Al concentration achieved in the films was 7.9 at.%, whilst the maximum was 38.5 at.%. An AlN film was deposited for comparison purposes, reaching an almost stoichiometric composition. For easy coating identification, hereinafter, the films will be termed $Ti_{1-x}Al_xN$, where x is the ratio Al/(Al + Ti) in the films.

The structural evolution of the $Ti_{1-x}Al_xN$ films as a function of the x is depicted in Fig. 2. For x from 0.16 up to 0.36, TiAlN exhibits a NaCl-cubic crystal structure dominated by a (111) preferential orientation. The XRD diffraction peak of the film with x = 0.16 is shifted to lower angles concerning the reference ICDD TiN cubic phase, suggesting that the film is under a residual stress state. The relation between peak position and stress was observed by Liu et al. [18] for AlN. With increasing Al content (x = 0.21), the (111) diffraction peak shifts to higher angles and loses intensity, indicating a lattice shrinking due to the substitution of Ti by the smaller Al atoms [1]. With Al content above 0.30, the (200) diffraction peak is also detected, the (111) preferred orientation decreases, and for the 0.56 film, a random orientation is observed. The hexagonal AlN is formed for films with x ≥ 0.69 beyond the cubic phase. These results agree with the literature where when the Al content exceeds the maximum solubility (Xmax ~0.7), a mixture of the cubic-NaCl and wurtzite structures is formed [19,20]. The position of the prominent peak of the hcp phase to lower angles suggests the presence of Ti atoms in substitution of the smaller Al atoms [21]. The lattice constant was calculated based on the (111) peak of the cubic phase and the (100) peak of the hexagonal cell. For the (111) plane, the cubic lattice constant decreases with increasing the Al content from 4.279 down to 4.197 Å; Similarly, for the (100) plane, the hexagonal lattice constant decreases from 3.682 to 3.672 Å. The lattice constant evolution with Ti:Al ratio is shown in Fig. A1 (a) and (b) for the cubic and hexagonal lattice, respectively.

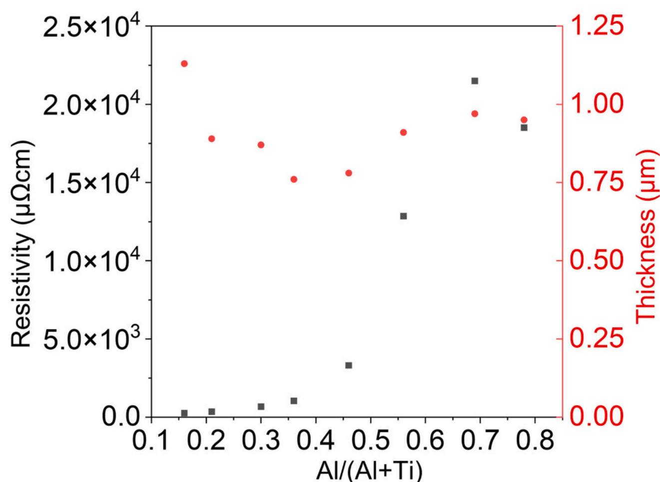

Fig. 3. Measured resistivity according to the Al content in $Ti_{1-x}Al_xN$ and thickness.

3.2. Electrical properties

Fig. 3 illustrates a plot of the TiAlN resistivity according to the chemical composition and thickness of the coatings. As expected, the samples positioned at the center of the substrate holder are thinner since their distance to the targets was higher; however, the difference between the lowest and highest values is slight (≈ 0.7–1.2 μm). The resistivity has a near-exponential increase with the rise of the Al content in the film, except for the sample with the highest Al content. It would be expected that the sample with the highest Al content would exhibit the highest resistivity, which was not the case. X-ray diffractograms show that AlN single phase is not achieved; samples with x = 0.78 and x = 0.69 are composed of two phases, h-AlN and c-TiN. Fujita et al. [3] did not find a steady increase in the resistivity for a similar range of compositions, and the amplitude is higher than the one presented in this study. Since a pure AlN phase is not achieved, Ti atoms may still be replacing Al atoms in the hexagonal lattice. The resistivity of the system could not exhibit a trend when the two phases are present in the mixture. Also, Kassavetis et al. [22] found resistivity variations in the transition zone from B1-TiAlN to the B4-TiAlN. Liu et al. [23] achieved a hcp single phase for x > 0.75 with a combinatorial deposition. However, the authors used a single target approach, which was not feasible for this study.

The range of measured resistivities (215–2.1 × 10^4 μΩcm) is coherent with values found in the literature for materials with a similar chemical composition [22,24,25].

The sheet resistance was measured up to 200 °C in air, and their evolution as a function of Al content is displayed in Fig. 4. For x = 0.16, the sample has a typical metallic behavior [26], where scattering events

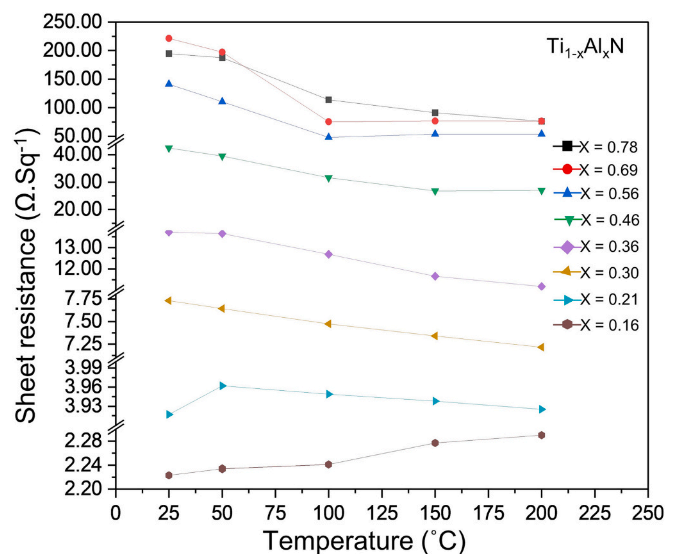

Fig. 4. Sheet resistance measurement with temperature for each chemical composition, from room temperature to 200 °C in air. The lines are only for the reader's guidance.

Table 3
Sensitivity, activation energy and TCR for each chemical composition. Sensitivity and TCR were calculated for [25–100 °C]. The activation energy was found from the linear dependence of lnRs vs 1000/T.

Al/(Al + Ti)	β (K)	E_a (meV)	TCR (°C^{-1})
0.16	–	–	1.1×10^{-4}
0.21	12.1	0.06	4.6×10^{-4}/-6.6×10^{-5}
0.3	50.3	4.75	-3.8×10^{-4}
0.36	116.9	15.22	-1.1×10^{-3}
0.46	437.2	41.28	-3.4×10^{-3}
0.56	1603.6	141.04	-8.8×10^{-3}
0.69	1595.3	142.93	-8.8×10^{-3}
0.78	794.8	70.32	-5.5×10^{-3}

reduce the electrons mobility due to lattice vibrations, promoted by the increase in thermal energy [4]. At low Al concentration, free electrons from Ti d orbitals are still available in sufficient number to explain the increase of resistance with temperature. The sample with x = 0.21 has distinct behaviors throughout the temperature range. Up to 50 °C, it behaves like a metallic, showing a positive slope (positive TCR), while above 50 °C, it shows a semiconductor behavior, showing a negative slope (negative TCR) [26]. Samples with x = 0.30, 0.36, 0.46 and 0.78 exhibit NTC semiconductor-like behavior, whilst samples with x = 0.56 and 0.69 show an inverse trend roughly at 100 °C, with a curve slope slightly positive up to 200 °C. This phenomenon is explained by the thermo-resistive effect in semiconductors [27]. As the temperature increases, the charge carriers concentration in the conduction band increases, decreasing the material's resistivity, which is visible from 25 to 100 °C. Above 100 and up to 200 °C, the concentration of free charge carriers from the extrinsic region stabilizes. Their mobility is reduced, giving rise to a slightly positive temperature coefficient (PTC) semiconductor-like behavior. This is usually named the saturation region and is essential in developing semiconductors that maintain their conductivity independently of temperature. It was not possible to resolve the sheet resistance for AlN due to its insulation properties.

The sensitivity, TCR and activation energy as a function of the chemical composition are listed in Table 3. As expected, β and TCR follow the same trend achieving the highest value for the compound $Ti_{1-x}Al_xN$, for x = 0.56, 0.69 (the values are comparable). The activation energy for conduction increases up to x = 0.56, 0.69, which suggests a decrease in the carrier density on the conduction band. On the other hand, the activation energy decreases in the sample with the highest x ratio. As stated before, the electrical properties of samples with x = 0.69 and x = 0.78 are somewhat scattered within this range due to the presence of two phases corresponding to h-AlN and c-TiN. The observed metallic region in Fig. 4 at temperatures above 100 °C for samples with x = 0.56 and x = 0.69 highlights the role of the activation energy of free carriers in TiAlN samples on their electrical behavior.

The table also shows the possibility of tuning the electrical properties of the TiAlN through chemical composition [22,23] and that the binary phase separation of the TiAlN did not improve the behavior in relation to the thermo-resistive properties. The best value achieved for sensitivity is not comparable with the high values given for Mn-based metal oxides films [10,11,15]. Despite this, the results are aligned with the ones from the study by the Mitsubishi researchers, except for the TiAlN in the wurtzite phase [3].

3.3. Chemical states

The cubic phase of the metastable TiAlN solid solution is characterized by having the best mechanical and wear properties. The absence of the hexagonal phase delays the spinodal decomposition in their stable binary compounds with temperature, c-TiN and h-AlN, maintaining thermal stability at high temperatures [1,19,20]. The two TiAlN films with cubic phase and the highest sensitivities achieved in the present study are those with compositions x = 0.46 and 0.56. However, to proceed with XPS, the resistance trend with temperature in the sample with x = 0.46 does not present the saturation region, which is the desired behavior for temperature sensors. Therefore, XPS was only performed in the sample with x = 0.46. Similar characterization was performed in the AlN sample for comparison purposes. The XPS HR spectra (Ti, Al, N, O, C) for the sample $Ti_{1-x}Al_xN$ (x = 0.46) are shown in Fig. 5 with the respective comparison with the AlN ones.

In the Ti 2p spectra, the spin-orbit splitting doublets Ti $2p_{3/2}$ and Ti $2p_{1/2}$ are visible, with a spacing between them around 5.7–6.15 eV, which is typical for this element. Three oxidation states were assigned for Ti: at 454.9, 456.4 and 458.2 eV corresponding to Ti^{2+}, Ti^{3+} and T^{4+}, respectively [21,27,28]. The Ti oxidation state peaks displayed in the plot match the equivalent compound, particularly TiO, TiN and TiO_2, respectively. The literature presents the TiO compound at different binding energies (BE), including the 455.1 value [28]. Since this peak has the lowest BE and knowing that no ion cleaning of the surface was performed, it can be associated with adsorbed oxygen bonded to Ti at the surface. Ti^{3+} and Ti^{4+} peaks are positioned in the BE assigned to TiN and TiO_2 [21,28]. The prominent peaks in the Al 2p spectra are assigned to AlN at 73.5 eV [21,27,28]. The small peaks placed at higher BE can be associated with the Al—O bond, again resulting from the adsorption of O to the surface. Comparing the TiAlN and AlN elements spectra, as expected, the intensity of the Al 2p peak is much higher for the AlN sample. Three prominent peaks in the N 1S spectra are observable: the peaks positioned at 395.8 and 396.8 eV can be assigned to metal nitrides, corresponding to TiN and AlN [27–30], respectively. The peak at 398.4 eV can be regarded as impurities or organics [21,28,31].

The O 1S spectrum presents two peaks at 530 and 531.8 eV and can be assigned to metal oxides and organics C—O bonding (adventitious contamination), respectively [27,28,32]. The metal oxide bond can be ascribed to Al^{3+}, Ti^{2+} and Ti^{4+} [21,27,28]. The C 1S spectra present three peaks at 284.8, 286.4 and 288.7 eV. The first peak can be assigned to C—C surface contamination (which served as a reference for the correction of peaks positions) [28,31], and the small peaks at 286.4 and 288.7 eV can be ascribed to C—O and C═O bonding [28,31,32]. The chemical bonds found for carbon and oxygen are somewhat expected since the samples were not physically etched and cleaned of possible surface contaminants before XPS acquisition. The difference in peak intensity for C and O between TiAlN and AlN is irrelevant since the elements should be segregated on the surface and not homogeneously distributed.

The XPS results show N—Ti and N—Al bonds and the inevitable surface oxidation promoted by the exposure of the samples to air. As a result, Ti oxidation states, Ti^{4+} and Ti^{2+}, have no significant relevance in the conduction mechanism. On the other hand, the higher intense peak Ti^{3+} from the Ti—N bond demonstrates that Ti has a free electron from the d_{xy} orbital that can contribute to the electrical conduction mechanism [24,26]. This agrees with the increased activation energy while the amount of Ti decreases (see Table 3, exception for x = 0.78), which means fewer free electrons at the donor level.

3.4. Electrical impedance spectroscopy, EIS, analysis

The AC impedance was performed on the same sample selected for the XPS analysis. This method allows the identification of the different

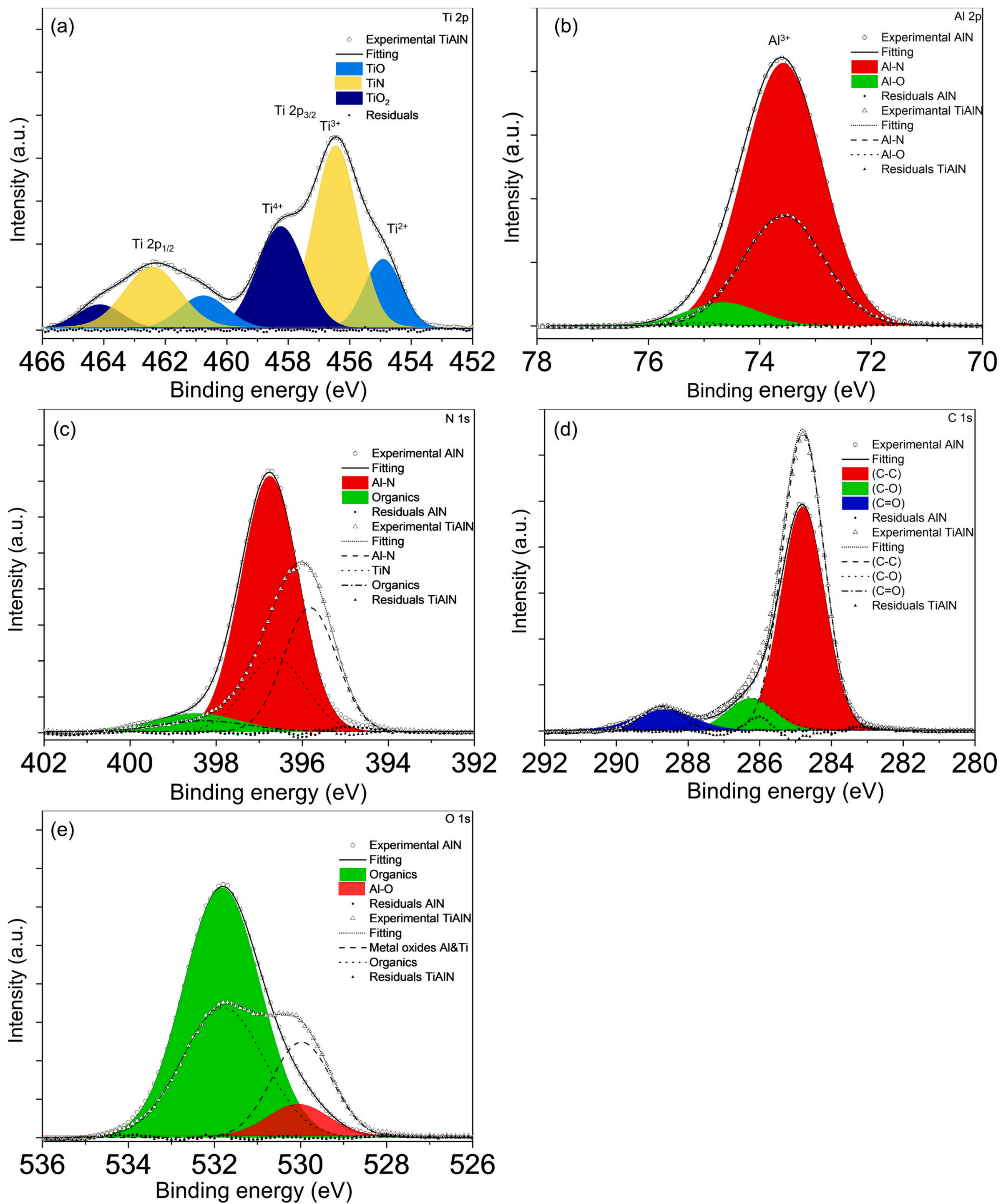

Fig. 5. XPS spectra comparing samples $Ti_{1-x}Al_xN$ for x = 0.46 and AlN displaying HR spectra for Ti 2p (a), Al 2p (b), N 1s (c) C 1s (d) and O 1s (e). Residuals are shown in the spectra, and a Shirley background was used for peak fitting.

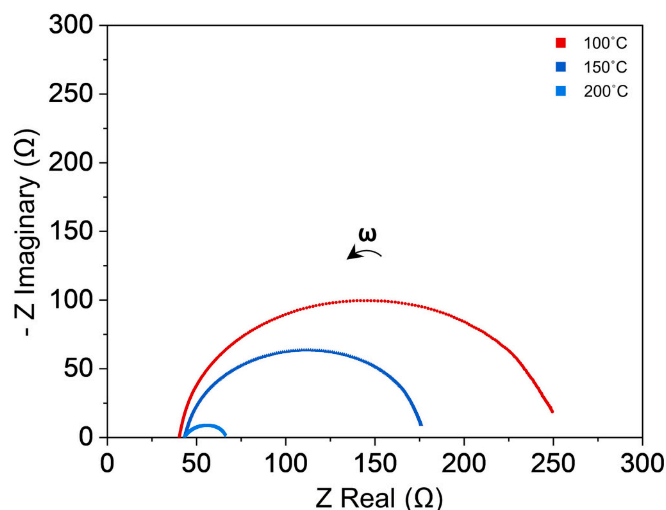

Fig. 6. Representation of Nyquist plots for sample $Ti_{1\text{-}x}A_xlN$, x = 0.46: temperatures tested 100 (red line), 150 (blue line) and 200 °C (light blue line).

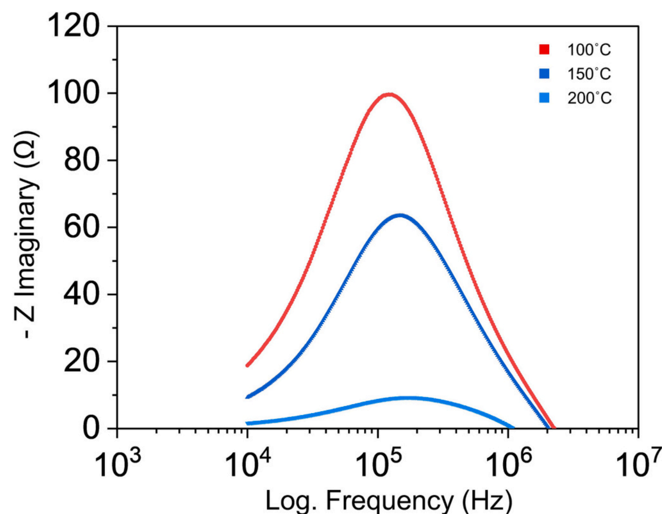

Fig. 7. Imaginary part as a function of frequency for different temperatures for samples $Ti_{1\text{-}x}A_xlN$, x = 0.46: temperatures tested 100 (red line), 150 (blue line) and 200 °C (light blue line).

contributions to the electrical response. To proceed with EIS analysis, two electrodes (silver epoxy glue) were applied on the sample to measure the impedance at 100, 150 and 200 °C. Fig. 6 shows the complex impedance spectra (Nyquist diagrams) for the selected TiAlN sample for diverse testing temperatures. Generally, in an ideal polycrystalline material, the conduction mechanisms in Nyquist plots are represented by semi-circles attributed to the grain boundary, grain and electrode polarization, from low to mid and high-frequency, respectively [12,33]. Equivalent circuit elements can modulate the diagrams to fit the curves representing different phenomena contributing to the overall conduction and polarization processes (see Fig. 8). The Nyquist plot for the AlN sample is not defined since it does not contain relevant information; it is composed only of a straight line, overlapping the real axis, not containing a reactive component in agreement with its electrical insulating character.

Through the analysis of the complex spectra, it is possible to realize that the resistance of the electrodes plus the system wiring, measured from the left interception of the depressed semi-circles with the real axis (high-frequency limit), is comparable for both samples and close to 45 Ω (see Table 4). Similarly, the grain resistance contribution is smaller than the grain boundary one since the depressed semi-circles do not intercept the real axis at low frequencies [13].

The imaginary part of the impedance-stimulus frequency, shown in Fig. 7, also confirms the claim. The time constant peak (relaxation frequency) at 100 °C is slightly shifted to lower frequencies. As a result, the conduction mechanism is dominated by electron hopping, which occurs between grains, overcoming the resistivity from the grain boundary [34]. According to Yoshikawa et al. [4], this type of conduction on TiAlN occurs at low temperatures. As already stated, the grain contribution is a non-dominant mechanism regarding the overall electrical response. However, since there is a peak shift to higher frequencies as the temperature rises (Fig. 7), it can be concluded that there is also an increase in the grain effect, i.e., the bulk effect gains an increased relevance that can be credited to conduction band [12]. The sample reveals an NTC

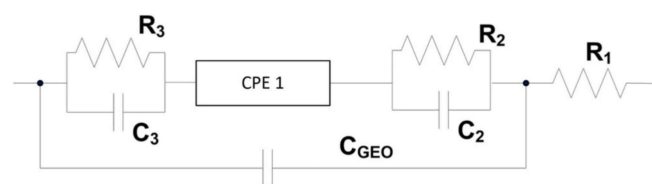

Fig. 8. Equivalent circuit model.

thermistor behavior above 100 °C once it shows the decrease in total impedance.

It is known that the impedance spectra illustrate the diverse polarization and electrical phenomena that contribute to the overall response of the materials. More than one equivalent circuit can fit the obtained data with a satisfactory result. The selection between these circuits must be based on simplicity and consistency with the known physical and chemical phenomena [35]. So, following the spectra analysis, a model of an equivalent circuit was developed and illustrated in Fig. 8.

The initial values of the components in the model were obtained using EIS spectra analyzer software, followed by their manual fine-tuning. In the proposed model, the following contributions were considered: 1) R_1 stands for the electrodes and measuring system wiring resistance; 2) the constant phase element, CPE1, represents the inhomogeneities in the interface between electrodes and the material, and along the surface of the sample. The CPE impedance is defined as $1/(Q(j\omega)^n$, where Q is the admittance when $\omega = 1$ rad/s, and $0 < n < 1$, which allows the CPE to be partly capacitive when n approaches one or partly resistive when n approaches to 0 [36]; 3) the two elements $R_2//C_2$ and $R_3//C_3$, composed of a resistor in parallel with a capacitor, represent the bulky granular and grain boundaries contributions, respectively; 4) the geometric capacitance, C_{GEO}, stands for the geometric effects contribution of the electrodes location, which are placed on the extremities of the upper faces of the samples and, consequently, the measuring configuration exhibits a shape that has similarities to the one of a capacitor with

Table 4
Circuit model fitted parameters for sample $Ti_{1\text{-}x}Al_xN$ with x = 0.46.

Temperature (°C)	R_1 (Ω)	R_2 (Ω)	C_2 (F)	R_3 (Ω)	C_3 (F)	C_{GEO} (F)	Q (Ω^{-1})	n (a.u)
100	40.8	200	3.55×10^{-10}	300	9.33×10^{-6}	6.5×10^{-9}	1.02×10^{-4}	0.55
150	44	125	3.55×10^{-10}	300	1.33×10^{-5}	8.6×10^{-9}	6.02×10^{-5}	0.605
200	43.4	12.7	5.5×10^{-8}	300	1.33×10^{-4}	4.59×10^{-8}	8.02×10^{-6}	0.9

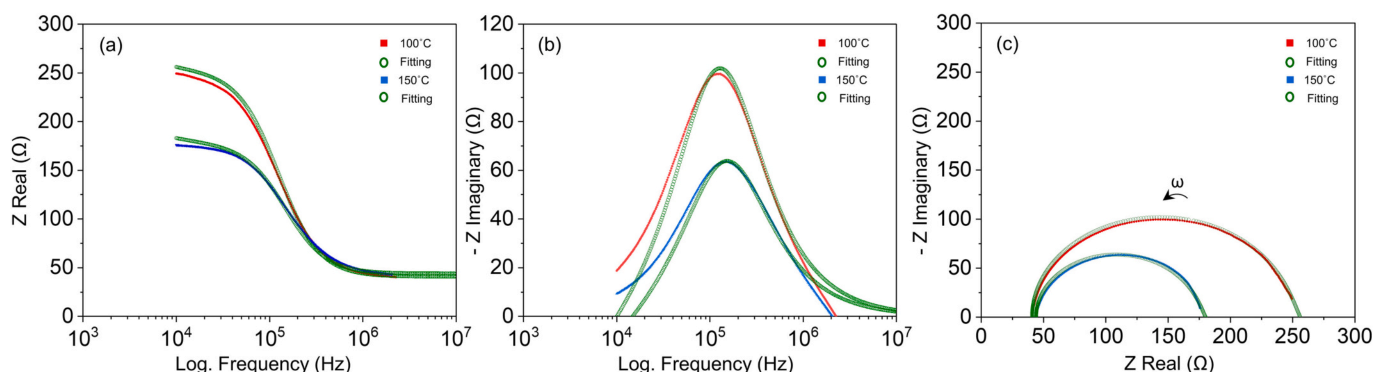

Fig. 9. Examples of fits using the equivalent model for sample $Ti_{1-x}A_xlN$, with x = 0.46 at the tested temperatures, 100 and 150 °C (plots (a), (b) and (c) – Real-Frequency; Imaginary-Frequency; Nyquist).

parallel plates, with the under test material in-between the plates. Fig. 9 shows some examples of the fits performed using the proposed model. From the plotted fittings, the adequation of the equivalent model studied and developed can be confirmed. Indeed, the Nyquist and Bode fit agree well with the experimental data.

The values which better represent the overall electrical response of the sample $Ti_{1-x}Al_xN$ (x = 0.46) are presented in Table 4 The CPE components (Q, n) reveal the increase of the capacitive part of the impedance, which could be related to a slight uncoupling of the silver electrodes from the sample surface as the temperature increases. The total resistance ($R_2 + R_3$) decreases with temperature, a characteristic feature of materials with NTC behavior. Considering the resistance of the grain boundaries (R_3), its value is maintained up to 200 °C, but the influence of the charge transfer is low when compared with the charge separation coming from the capacitive effect (C_3); Since they are in parallel, they occur at the exact spatial location. In contrast, the capacitive effect at the grain has less impact, highlighting the effects of the charge transfer derived from resistance R_2. The time constants (T = C × R) increase with temperature for grain and grain boundary contribution, i.e., the characteristic frequency for each contribution (f = 1/T) decreases. The fitted data follows the peak shifting observed in Fig. 7, which demonstrates the increasing role of the grain with temperature. For instance, at 200 °C, the characteristic frequency for the grain boundary is 4 Hz, whereas the grain is 2.3×10^5 Hz, close to the relaxation peak frequency of 1.79×10^5 Hz.

4. Conclusions

In this work, TiAlN thin films with different Ti/Al ratios were produced by combinatorial deposition using Ti and Al targets.

In the range $0.16 \leq x \leq 0.56$, $Ti_{1-x}Al_xN$ films displayed a single-phase NaCl-type structure as a metastable solid solution of Al in the TiN lattice. Two phases (c-TiN and h-AlN) are formed for $x \geq 0.69$. TiAlN shows a maximum resistivity of 2.1×10^4 μΩcm at x = 0.69 and NTC-type thermistor characteristics for $x \geq 0.21$. Furthermore, in the range $0.56 \leq x \leq 0.69$, the semiconductive thermo-resistive effect is revealed by showing extrinsic and metal-like regions with the temperature increase. The compositions x = 0.56 and x = 0.69 show similar behavior with the highest TCR ≈ 8.8×10^{-3} °C^{-1} and β ≈ 1600 K values.

The XPS revealed the presence of Ti—N bonding for the composition x = 0.46 showing the availability of a free electron from Ti. For the same ratio, the EIS measurements show the relevance of the grain boundary effect in the conduction mechanism. Hence, it is suggested that the conduction mechanism for this composition is, up to 200 °C, based on electron hopping promoted by Ti unbound electrons and grain boundaries as the primary energy barrier. In addition, 200 °C should be the onset temperature for long-range conduction, i.e., in the intrinsic semiconductor region. The shift and broadening of the relaxation time peaks to high frequencies support the findings by showing the increasing effect of the grain close to 200 °C.

Finally, it was demonstrated that it is possible to develop TiAlN thin films by sputtering that can be used as thermistor sensors. The maximum β found is not close to the sensitivities of oxide's thermistors; however, R25 is easily tuned based on the resistor's design rules and the sheet resistance of the material.

Supplementary data to this article can be found online at https://doi.org/10.1016/j.surfcoat.2023.129545.

CRediT authorship contribution statement

Bruno Martins: Investigation, Writing – original draft, Visualization. **Carlos Patacas:** Investigation, Visualization. **Albano Cavaleiro:** Writing – review & editing, Supervision, Validation, Conceptualization. **Pedro Faia:** Investigation, Writing – review & editing. **Oleksandr Bondarchuk:** Investigation. **Filipe Fernandes:** Writing – review & editing, Supervision, Validation, Conceptualization.

Declaration of competing interest

The authors declare that they have no known competing financial interests or personal relationships that could have appeared to influence the work reported in this paper.

Data availability

Data will be made available on request.

Acknowledgements

This research is sponsored by national funds: Soft4Sense project "Smart Surfaces for Reliable Tooling Integration" (reference: POCI-01-0247-FEDER-045921), co-financed by the European Regional Development Fund, through Portugal 2020 (PT2020), by the Competitiveness and Internationalization Operational Programme (COMPETE 2020) and Foundation for Science and Technology (FCT) is also acknowledged.

References

[1] M. Danek, F. Fernandes, A. Cavaleiro, T. Polcar, Influence of cr additions on the structure and oxidation resistance of multilayered TiAlCrN films, Surf. Coat. Technol. 313 (2017) 158–167, https://doi.org/10.1016/j.surfcoat.2017.01.053.
[2] U. Ratayski, M. Motylenko, A. Ershova, M. Šíma, M. Jílek, D. Rafaja, Competition between local lattice strains and distribution of metallic species in ti 1–x Al x N coatings with fluctuating [Ti]/[Al] ratio, Surf. Coat. Technol. 344 (2018) 322–329, https://doi.org/10.1016/j.surfcoat.2018.03.031.
[3] T. Fujita, H. Tanaka, H. Inaba, N. Nagatomo, Development and electrical properties of wurtzite (Al, Ti)N materials for thin film thermistors, J. Ceram. Soc. Japan. 124 (2016) 653–658, https://doi.org/10.2109/jcersj2.15316.

[4] M. Yoshikawa, D. Toyama, T. Fujita, N. Nagatomo, T. Makimoto, Hole conduction characteristics of cubic Ti1−xAlxN, Thin Solid Films 660 (2018) 711–714, https://doi.org/10.1016/j.tsf.2018.04.010.

[5] S. Suzuki, T. Fujita, Y. Hosokawa, K. Fujiwara, N. Nagatomo, Development of a wurtzite (Al, Ti)N thermistor on a resin substrate with high heat resistance, J. Ceram. Soc. Japan. 129 (2021) 355–358, https://doi.org/10.2109/jcersj2.20224.

[6] N. Inaba, Nagatomo Hitoshi, Temperature Sensor, EP2902761B1, 2012.

[7] H. Inaba, Nagatomo Hitoshi, Tanaka Noriaki, Temperature sensor and method for producing same, US10113919B2, 2012.

[8] H. Inaba, K. Kubota, N. Nagatomo, H. Tanaka, Film-type Thermistor Sensor, US2015055682A1, 2012.

[9] B. Yang, M. He, K. Wen, D. Xiong, Y. Feng, S. Ta, Z. Yang, Comparison of morphology, electrical properties and sensitivity between bulk and thin-film Mn1.5Co1Ni0.5O4 thermistors, Ceram. Int. 46 (2020) 27134–27142, https://doi.org/10.1016/j.ceramint.2020.07.192.

[10] W. Kong, J. Wang, J. Yao, A. Chang, Influence of oxygen atmosphere annealing on the thermal stability of Mn1.2Co1.5Ni0.3O4±δ ceramic films fabricated by RF magnetron sputtering, Ceram. Int. 44 (2018) 1455–1460, https://doi.org/10.1016/j.ceramint.2017.10.040.

[11] T. Xuan, J. Yan, J. Wang, W. Kong, A. Chang, Characterization of Al-doped Mn–Co–Ni–O NTC thermistor films prepared by the magnetron co-sputtering approach, J. Alloys Compd. 831 (2020), 154831, https://doi.org/10.1016/j.jallcom.2020.154831.

[12] X. Sun, H. Zhang, Y. Liu, J. Guo, Z. Li, Characterization of new negative temperature coefficient thermistors based on Zn–Ni–O system, J. Adv. Ceram. 5 (2016) 329–336, https://doi.org/10.1007/s40145-016-0206-0.

[13] Q. Ruifeng, X. Fu, Z. Zou, W. Zheng, L. Luo, Yan, mn-co-ni-O thin films prepared by sputtering with alloy target, J. Adv. Ceram. 9 (2020) 64–71, https://doi.org/10.1007/s40145-019-0348-y.

[14] Q. Shi, W. Ren, W. Kong, B. Gao, L. Wang, C. Ma, A. Chang, L. Bian, High B value Mn-Co-Ni spinel films on alumina substrate by RF sputtering, J. Mater. Sci. Mater. Electron. 28 (2017) 9876–9881, https://doi.org/10.1007/s10854-017-6742-8.

[15] Y. Yin, J. Wu, W. Zhou, L. Jiang, Z. Huang, Post annealing effects on low temperature deposited Mn-Co-Ni-O films by radio frequency magnetron sputtering, Mater. Lett. 235 (2019) 172–175, https://doi.org/10.1016/j.matlet.2018.10.046.

[16] K. Strijckmans, R. Schelfhout, D. Depla, Tutorial: hysteresis during the reactive magnetron sputtering process, J. Appl. Phys. 124 (2018), 241101, https://doi.org/10.1063/1.5042084.

[17] I. Miccoli, F. Edler, H. Pfnür, C. Tegenkamp, The 100th anniversary of the four-point probe technique: the role of probe geometries in isotropic and anisotropic systems, J. Phys. Condens. Matter. 27 (2015), 223201, https://doi.org/10.1088/0953-8984/27/22/223201.

[18] H.Y. Liu, G.S. Tang, F. Zeng, F. Pan, Influence of sputtering parameters on structures and residual stress of AlN films deposited by DC reactive magnetron sputtering at room temperature, J. Cryst. Growth 363 (2013) 80–85, https://doi.org/10.1016/j.jcrysgro.2012.10.008.

[19] Y. Pinot, M.H. Tuilier, M.J. Pac, C. Rousselot, D. Thiaudière, C. Ulhaq-Bouillet, Influence of film thickness on the structural transition cubic/hexagonal within Ti0.38Al0.62N films, Thin Solid Films 649 (2018) 160–166, https://doi.org/10.1016/j.tsf.2018.01.024.

[20] F.C. Yang, C.Y. Lin, J.F. Tang, C.L. Chang, Effect of mid-frequency pulse insertion on the microstructural and mechanical properties of AlTiN coatings prepared using superimposed HiPIMS process, Surf. Coat. Technol. 388 (2020), 125597, https://doi.org/10.1016/j.surfcoat.2020.125597.

[21] G. Xian, H.B. Zhao, H.Y. Fan, H. Du, Structure and mechanical properties of Zr/TiAlN films prepared by plasma-enhanced magnetron sputtering, Rare Metals 34 (2015) 717–724, https://doi.org/10.1007/s12598-014-0300-9.

[22] S. Kassavetis, G. Abadias, G. Vourlias, G. Bantsis, S. Logothetidis, P. Patsalas, Optical properties of TixAl1 − xN thin films in the whole compositional range, Surf. Coat. Technol. 295 (2016) 125–129, https://doi.org/10.1016/j.surfcoat.2015.08.049.

[23] S. Liu, K. Chang, S. Mráz, X. Chen, M. Hans, D. Music, D. Primetzhofer, J. M. Schneider, Modelling of metastable phase formation for sputtered Ti1-xAlxN thin films, Acta Mater. 165 (2019) 615–625, https://doi.org/10.1016/j.actamat.2018.12.004.

[24] I. Krylov, Y. Qi, V. Korchnoy, K. Weinfeld, M. Eizenberg, E. Yalon, Zero temperature coefficient of resistance in back-end-of-the-line compatible titanium aluminum nitride films by atomic layer deposition, Appl. Phys. Lett. 117 (2020) 0–5, https://doi.org/10.1063/5.0012739.

[25] R. Rachbauer, J.J. Gengler, A.A. Voevodin, K. Resch, P.H. Mayrhofer, Temperature driven evolution of thermal, electrical, and optical properties of ti-Al-N coatings, Acta Mater. 60 (2012) 2091–2096, https://doi.org/10.1016/j.actamat.2012.01.005.

[26] I. Krylov, V. Korchnoy, X. Xu, K. Weinfeld, E. Yalon, D. Ritter, M. Eizenberg, Electrical and structural properties of conductive nitride films grown by plasma enhanced atomic layer deposition with significant ion bombardment effect, J. Appl. Phys. 128 (2020), 065301, https://doi.org/10.1063/5.0015961.

[27] T. Dinh, H.P. Phan, A. Qamar, P. Woodfield, N.T. Nguyen, D.V. Dao, Thermoresistive effect for advanced thermal sensors: fundamentals, design considerations, and applications, J. Microelectromech. Syst. 26 (2017) 966–986, https://doi.org/10.1109/JMEMS.2017.2710354.

[28] C. Badini, S. Deambrosis, E. Padovano, M. Fabrizio, O. Ostrovskaya, E. Miorin, G. D'Amico, F. Montagner, S. Biamino, V. Zin, Thermal shock and oxidation behavior of HiPIMS TiAlN coatings grown on ti-48Al-2Cr-2Nb intermetallic alloy, Materials (Basel). 9 (2016) 961, https://doi.org/10.3390/ma9120961.

[29] J.F. Moulder, Handbook of X-ray Photoelectron Spectroscopy: A Reference Book of Standard Spectra for Identification and Interpretation of XPS Data, Physical Electronics Division, Perkin-Elmer Corporation, 1992.

[30] E. Lewin, J. Patscheider, Structure and properties of sputter-deposited Al-sn-N thin films, J. Alloys Compd. 682 (2016) 42–51, https://doi.org/10.1016/j.jallcom.2016.04.278.

[31] I. Bertóti, Characterization of nitride coatings by XPS, Surf. Coat. Technol. 151–152 (2002) 194–203, https://doi.org/10.1016/S0257-8972(01)01619-X.

[32] M. Nose, T. Kawabata, S. Khamseh, K. Matsuda, K. Fujii, S. Ikeno, W.A. Chiou, Microstructure and properties of TiAIN/a-C nanocomposite coatings prepared by reactive sputtering, Mater. Trans. 51 (2010) 282–287, https://doi.org/10.2320/matertrans.MC200913.

[33] Table of Elements | Thermo Fisher Scientific, (n.d.). https://www.thermofisher.com/pt/en/home/materials-science/learning-center/periodic-table.html.

[34] G. Zhan, Z. Lin, B. Xu, J. Feng, B. Yang, X. Chen, C. Yang, J. Liu, Study of temperature sensitivity and impedance spectroscopy of zirconium oxynitride thin film thermistors, J. Mater. Sci. Mater. Electron. 28 (2017) 9653–9657, https://doi.org/10.1007/s10854-017-6715-y.

[35] J.E. Bauerle, Study of solid electrolyte polarization by a complex admittance method, J. Phys. Chem. Solids 30 (1969) 2657–2670, https://doi.org/10.1016/0022-3697(69)90039-0.

[36] K. Fujiwara, S. Lee, N. Donnelly, T. Yamaguchi, C.A. Randall, Resistance degradation in Y(Cr, Mn)O3–Y2O3 composite NTC ceramics in hostile environments, J. Am. Ceram. Soc. 92 (2009) 2634–2641, https://doi.org/10.1111/j.1551-2916.2009.03253.x.